



HAL
open science

BaTiO₃-Gd₃Fe₅O₁₂ Composites: Exploring the Dielectric Properties in a Broad Frequency Range

Bruno M. G. Melo, Clara Baivier, Ratiba Benzerga, Didier Fasquelle, S. Soreto Teixeira, Manuel P F Graça, Luís Costa

► **To cite this version:**

Bruno M. G. Melo, Clara Baivier, Ratiba Benzerga, Didier Fasquelle, S. Soreto Teixeira, et al.. BaTiO₃-Gd₃Fe₅O₁₂ Composites: Exploring the Dielectric Properties in a Broad Frequency Range. Crystals, 2024, 14 (7), pp.590. 10.3390/cryst14070590 . hal-04649537

HAL Id: hal-04649537

<https://hal.science/hal-04649537>

Submitted on 16 Jul 2024

HAL is a multi-disciplinary open access archive for the deposit and dissemination of scientific research documents, whether they are published or not. The documents may come from teaching and research institutions in France or abroad, or from public or private research centers.

L'archive ouverte pluridisciplinaire **HAL**, est destinée au dépôt et à la diffusion de documents scientifiques de niveau recherche, publiés ou non, émanant des établissements d'enseignement et de recherche français ou étrangers, des laboratoires publics ou privés.



Distributed under a Creative Commons Attribution 4.0 International License

Article

BaTiO₃—Gd₃Fe₅O₁₂ Composites: Exploring the Dielectric Properties in a Broad Frequency Range

Bruno M. G. Melo ^{1,*}, Clara Baivier ², Ratiba Benzerga ², Didier Fasquelle ³, S. Soreto Teixeira ¹,
Manuel P. F. Graça ¹ and Luís Costa ¹

¹ i3N and Department of Physics, University of Aveiro, 3810-193 Aveiro, Portugal; silvia.soreto@ua.pt (S.S.T.); mpfg@ua.pt (M.P.F.G.); kady@ua.pt (L.C.)

² CNRS, IETR—UMR 6164, University of Rennes, 35000 Rennes, France; clara.baivier@etudiant.univ-rennes.fr (C.B.); ratiba.benzerga@univ-rennes.fr (R.B.)

³ UDSMM, Université du Littoral Côte d'Opale, 50, Rue Ferdinand Buisson, B.P. 717, 62228 Calais CEDEX, France; didier.fasquelle@univ-littoral.fr

* Correspondence: bmelo@ua.pt

Abstract: This study presents the dielectric properties of a barium titanate–gadolinium ferrite composite material, obtained through a solid-state reaction method. The aim of this research was to create a composite material with enhanced dielectric properties compared to each individual component, and to investigate the electrical properties of the composites, using impedance spectroscopy. The structural and morphologic properties were analyzed using X-ray diffraction and scanning electron microscopy, respectively. Impedance spectroscopy measurements were performed over a wide frequency range (100–0.1 GHz) and temperature (45–170 °C) to evaluate the electrical behavior of the material. The dielectric relaxations were analyzed using the Havriliak–Negami function, and the key electrical parameters such as relaxation frequency, dielectric strength, and electrical conductivity were extracted. Several relaxation processes were identified, which depend on the mixture of the initial titanate and ferrite materials, and a correlation between structural, morphologic, and electrical properties was exposed. The sample with the highest dielectric constant was the 25 wt% gadolinium ferrite composite, with ϵ' close to 240 and loss tangent values below 0.1, affording it the more appropriate composition for energy storage devices such as lead-free dielectric capacitors.



Citation: Melo, B.M.G.; Baivier, C.; Benzerga, R.; Fasquelle, D.; Teixeira, S.S.; Graça, M.P.F.; Costa, L. BaTiO₃—Gd₃Fe₅O₁₂ Composites: Exploring the Dielectric Properties in a Broad Frequency Range. *Crystals* **2024**, *14*, 590. <https://doi.org/10.3390/cryst14070590>

Received: 30 May 2024

Revised: 21 June 2024

Accepted: 25 June 2024

Published: 27 June 2024



Copyright: © 2024 by the authors. Licensee MDPI, Basel, Switzerland. This article is an open access article distributed under the terms and conditions of the Creative Commons Attribution (CC BY) license (<https://creativecommons.org/licenses/by/4.0/>).

Keywords: impedance spectroscopy; ceramic composites; Havriliak–Negami; dielectric materials; barium titanate

1. Introduction

Impedance spectroscopy is a powerful technique that allows for studying the electrical conductivity and polarization mechanisms of materials, related to charge migration and the orientation of permanent dipoles. To obtain a complete characterization of the dielectric response, a broad range of frequencies and temperatures must be used. The different regimes of the dielectric function can be observed and the dynamics of the relaxations can be found. In this case, a broad range in temperature and frequencies allows us to see the different relaxation processes present in the material [1].

In the field of electronics, the efficiency of devices for energy storage becomes imperative, not only for size and weight reduction but also for greater sustainability in the process, as fewer resources are consumed. When it comes to energy storage devices for electronics, capacitors are the most used, with various manufacturing technologies available depending on their intended use, considering energy density, size, and cost. The criteria for the materials used in capacitors encompass the need to have a high dielectric constant with minimal dielectric losses, a low leakage current, a substantial breakdown voltage, and adequate stability [2,3]. In addressing material challenges, the focus is on dielectric materials with dielectric constants exceeding 1000 [4,5] and exceptionally low dielectric

loss. Commonly, a dissipation factor below 0.1% is deemed highly favorable, while a factor as high as 5% is considered less desirable [4].

Barium titanate (BaTiO_3) is a well-known ferroelectric material, with a perovskite crystal structure and the capacity to polarize spontaneously, which can be reversed through the application of an electric field. This material is suitable for several applications in electronics, including capacitors that can store and release electrical energy, resonators, and tunable RF filters, among others [6]. Specifically, barium titanate capacitors are more suitable for applications that require high dielectric constants, a high energy storage density, and the ability to tolerate high temperatures [7]. They are used in fields like electronics, telecommunications, and aerospace where these properties are advantageous [7].

BaTiO_3 can be synthesized through various methods, including sol-gel, solid-state reaction, hydrothermal, and chemical vapor deposition [8]. The resulting physical properties can be modified by changing the preparation process parameters and the material's composition. Similarly, this compound opens the door to the creation of novel microstructures exhibiting multiferroic properties by incorporating other elements or particles into its matrix, such as ferrites [9].

Several doped BTO ceramics have been reported for use in energy storage. For example, Sm^{3+} -doped BTO ceramics showed better dielectric properties when compared with pure BTO ceramics [10]. Other trivalent ions' doping was also studied with promising dielectric properties. These include La^{3+} , Ce^{3+} , Dy^{3+} , and Nd^{3+} , with only small amounts of doping [11]. Kai Zhang et al. has shown that Yb^{3+} -doped BTO-based ceramic has a relatively good comprehensive performance with a high dielectric constant and low dielectric loss, with the potential for energy storage [12]. Other possibilities include Nb^{5+} - and/or In^{3+} -doped BTO, which were prepared by a conventional solid-state method, followed by annealing in N_2 , with interesting results [13].

That is, the dielectric properties can be improved by doping BaTiO_3 (BTO) with some rare earth oxides. The modified BTO can achieve a higher dielectric constant and also a higher breakdown electric field strength [14,15]. As observed, rare earth oxides, namely the rare earth ferrites, are particularly attractive due to their excellent dielectric properties, characterized by a high dielectric constant and minimal dielectric losses, showing potential to be candidates for electronic devices [16]. A distinguishing feature of iron garnets is the presence of exclusively trivalent cations, which impart high resistivity to these materials. Gadolinium ferrite $\text{Gd}_3\text{Fe}_5\text{O}_{12}$ (GIG) is one interesting example of an iron garnet. In these materials, dielectric losses are typically associated with the simultaneous presence of Fe^{2+} and Fe^{3+} ions occupying closely related crystallographic sites [17].

Given the inherent properties of both BTO and GIG, the objective of this study was to create a composite material with enhanced dielectric properties compared to each individual component. To achieve that objective, composites containing varying percentages of GIG were prepared, allowing for assessing the impact of gadolinium iron garnet (GIG) within a barium titanate (BTO) matrix and analyzing the resulting electrical properties.

2. Materials and Methods

In this study, both BaTiO_3 (BTO) and $\text{Gd}_3\text{Fe}_5\text{O}_{12}$ (GIG) powders, including composite materials, were prepared through a solid-state reaction process, followed by a sintering procedure. These compositions adhered to the formula $(100 - x) \text{BTO} + (x) \text{GIG}$, where x ranged from 0 to 100 wt%: 0, 25, 50, 75, and 100 wt%.

The initial step involved the preparation of BTO and GIG powders. Specifically, we created a mixture of high-purity BaCO_3 ($\geq 99.0\%$ purity, supplied by MaTeck, Jülich, Germany) and TiO_2 ($\geq 99.8\%$ purity, supplied by Sigma-Aldrich, St. Louis, MO, USA) at room temperature. To produce BaTiO_3 , the raw materials were weighed considering the stoichiometry of the reaction (1 mol (Ba^{2+}): 1 mol (Ti^{4+})). The synthesis of GIG was carried out using oxide powder of Fe_2O_3 ($\geq 99.0\%$ purity, supplied by Sigma-Aldrich, St. Louis, MO, USA) and gadolinium nitrate $\text{Gd}(\text{NO}_3)_3 \cdot 6\text{H}_2\text{O}$ ($\geq 99.0\%$ purity, supplied by Merck KGaA, Darmstadt, Germany), following the chemical equations and the same experimental

procedure to obtain the powders by solid-state reaction as were described in a previous work [18].

This work differed from the preceding one [18] in the thermal cycle given to the powders obtained from the solid-state reaction: in the current work, the heat treatment of the pellet samples was performed via a single-step sintering procedure, whereas the previous study involved a two-step sintering procedure. The scheme of the composites' experimental procedure is presented in Figure 1, while Table 1 summarizes the composites' initial composition from the BTO and GIG mixtures.

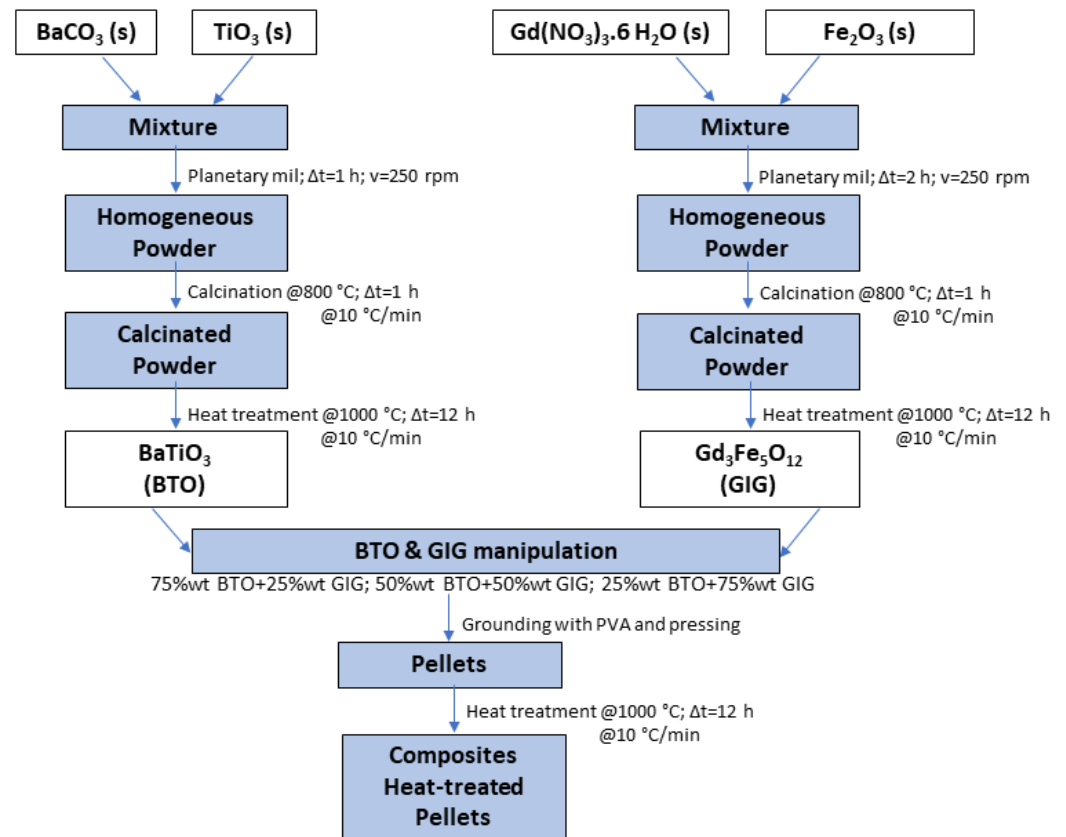


Figure 1. Scheme of the composite experimental procedure.

Table 1. BTO and GIG compositions of the as-prepared samples before the sintering procedure.

Sample	BaTiO ₃ (wt%)	Gd ₃ Fe ₅ O ₁₂ (wt%)
BTO	100	0
25GIG	75	25
50GIG	50	50
75GIG	25	75
GIG	0	100

In the current study, the dielectric behavior of the samples was studied in detail using the Havriliak–Negami model and correlated with the adopted thermal cycle.

The temperature of the heat treatments was selected from the thermal analysis discussed in [18], and was performed on the acquired powders using a differential thermal analysis (DTA) and thermogravimetry analysis (TGA) system, specifically the STA7300 Thermal Analysis System (HITACHI, Tokyo, Japan). The samples were subjected to a heat-

ing process, from 30 °C to 1200 °C, with a step of 10 °C per minute, which was accomplished under a nitrogen (N₂) atmosphere.

The powders underwent a calcination process at 800 °C in ambient air for 12 h, followed by X-ray diffraction analysis. After calcination, BTO and GIG powders were blended with ethanol using an agate mortar at room temperature to create three different compositions: 25%, 50%, and 75% GIG in the BTO matrix. To form pellets, each composition (composite) was mixed with an aqueous solution of polyvinyl alcohol (2 wt% of PVA dissolved at 80 °C) as a binding agent and pressed into cylindrical pellets 7 mm in diameter and around 1.3 mm in thickness, using a uniaxial pressure system and applying 3 MPa for 15 min. Subsequently, the pellets were sintered at 1000 °C, with a heating rate of 10 °C/min in an air environment for 12 h, and cooled to room temperature by the thermal inertia of the furnace. In this heat-treatment process the PVA binder was all removed. Additionally, reference pellets, i.e., without mixing the two base materials, were prepared by pressing BTO powder and GIG powder, using the same pressure and thermal conditions.

To evaluate the structural changes in the samples, namely, new crystal phases and the crystallographic parameters, X-ray diffraction (XRD) was performed by a diffractometer (PANalytical, AERIS) using Cu-K1 ($\lambda = 1.5406 \text{ \AA}$) at 40 kV and 15.0 mA. The XRD scans covered a 2θ angle range of 10°–70°, with a step size of 0.003°.

Furthermore, the cross-section morphology of the samples was analyzed by scanning electron microscopy (SEM) coupled with energy-dispersive X-ray spectroscopy (EDS), using a TESCAN Vega3 and a Bruker Nano X-Flash Detector 410-M, respectively. The SEM micrographs were acquired using an accelerated voltage of 30 kV. Prior to microscopic observation, the samples were coated with a carbon layer.

For the dielectric measurements at room temperature, two different impedance analyzers were used to cover the complete frequency range up to 0.1 GHz: a Keysight E4990A from 100 Hz to 1 MHz, and an HP4291A from 1 MHz to 0.1 GHz. For these measurements, cylindrical pellets (with a diameter of 7 mm and thickness close to 1 mm) were prepared by coating the opposite surfaces of the heat-treated pellets with silver conducting paste. The electrical measurements as a function of temperature were performed in a tubular furnace, across the frequency spectrum ranging from 100 Hz to 1 MHz, using an Agilent 4294A impedance analyzer, in the C_p—R_p configuration. The temperature of the sample was precisely controlled by a thermocouple placed close to the sample.

3. Results and Discussion

3.1. Thermal Analysis

In the results of previous work [18], for the DTA and TGA curves of BTO, there were significant changes around 900 °C. Meanwhile, for GIG, the previous results were not so conclusive; nevertheless, it is widely documented in the literature that the decomposition of transition metal nitrates, such as yttrium or gadolinium, typically occurs below 1000 °C [19]. Within the range of 500–600 °C, any remaining volatile products are expelled, resulting in the compound's mass reaching a near-constant level.

In alignment with previous results and based on the literature, we elected to perform the heat treatments of the BTO, GIG, and composite pellet samples at 1000 °C.

3.2. Structural Analysis

The crystalline structure of the samples was investigated by X-ray diffraction. Figure 2 shows the room temperature diffractograms and the Rietveld refinement of the base powders that were used to prepare the composites. The GIG sample was found to be a mixture of two phases, namely, Fe₂O₃ (ICDD pattern 04-008-7627) and Gd₃Fe₅O₁₂ (ICDD pattern 01-074-1361). The results obtained from the Rietveld refinement (Table 2) showed that the principal phase was Gd₃Fe₅O₁₂ (81 wt%). The results obtained from the Rietveld refinement (Table 2) showed that the principal phase was Gd₃Fe₅O₁₂ (81 wt%).

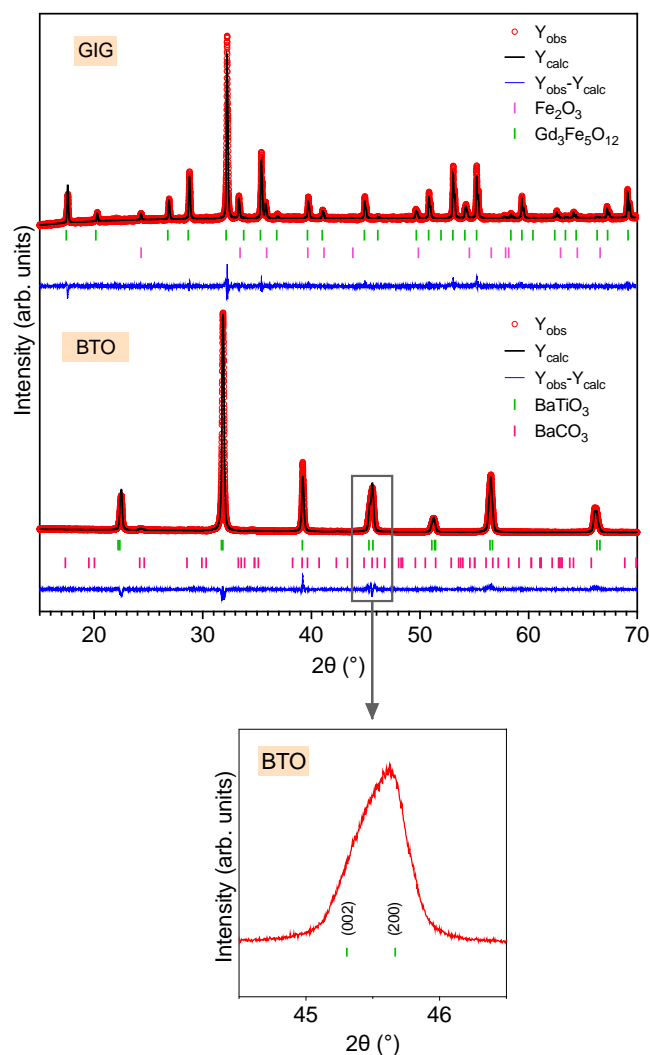


Figure 2. Rietveld refinement of the room temperature diffractogram from the powder samples GIG and BTO. The bottom figure shows an inset graphic of the BTO sample in the 2θ range of $44.5\text{--}46.5^\circ$.

Table 2. Results from the Rietveld refinement analysis for the GIG and BTO samples.

Sample	BaTiO ₃ (wt%)	BaCO ₃ (wt%)	Fe ₂ O ₃ (wt%)	Gd ₃ Fe ₅ O ₁₂ (wt%)	R _{exp}	R _p	R _{wp}	χ
GIG			18.60	81.40	2.10	2.00	3.95	1.88
BTO	98.61	1.39			5.46	6.39	8.11	1.49

For the BTO powder, the analysis of its diffractogram required additional care to identify the correct crystal system. It is well-known that, typically, BaTiO₃ has a tetragonal crystal system at room temperature [20–22]. However, depending on the synthesis route, the particle size can change significantly. As the BTO particle size decreases, the relative ratio of the cubic-to-tetragonal region is increased and eventually only a stable cubic region remains at a critical particle size [23]. A common way to identify its crystal system, cubic or tetragonal, is to evaluate the degree of peak separation between the (200) and (002) planes in the 2θ region between 44° and 47° . The peak splitting is representative of the tetragonal ferroelectric BaTiO₃ [22,24,25], while its absence indicates that the crystallites have a cubic structure [23,26]. As one can see in the inset of Figure 2, for the BTO sample, the diffraction peak at 45.5° is asymmetric, which could indicate a small split of the peak [25]. Nevertheless, it is not possible to distinguish between the (200) and the (002) peaks due to

their large overlap. This suggests that the tetragonal structure of BaTiO_3 is not perfectly formed in this sample, possibly due to the low annealing temperature. The tetragonality of the BTO sample, calculated from the ratio of lattice parameters of the c - to the a -axis, $=c/a$, is only 1.005. As discussed in [23], this low tetragonality is typical of BTO powders with an average particle size below 200 nm, in which no clear peak splitting is observed. Besides the tetragonal BaTiO_3 phase (ICDD pattern 04-006-9685), the BTO powder showed a minor secondary BaCO_3 phase (ICDD pattern 04-012-9372).

Figure 3 shows the room temperature diffractograms of the composite powder samples. Besides the BaTiO_3 tetragonal phase, the composite samples revealed the presence of two additional crystalline phases, namely, GdFeO_3 (ICDD pattern 04-015-5491) and $\text{BaFe}_7\text{O}_{12}$ (ICDD pattern 04-002-1982). While the base GIG powder was composed of Fe_2O_3 and $\text{Gd}_3\text{Fe}_5\text{O}_{12}$, the heat treatment performed at 1000 °C during the sintering step promoted the formation of these two new phases in the composite samples. As shown in Table 3, the weight percentage of the GdFeO_3 perovskite structure increases with the addition of GIG to the composites. For the sample with 25% GIG, the calculated wt% of GdFeO_3 was around 15% and the diffractogram showed some low-intensity peaks related to the $\text{BaFe}_7\text{O}_{12}$ phase. For the 50GIG sample, the amount of GdFeO_3 increases up to 33 wt%, and for the sample with 75% GIG, it became the major crystal phase with 55 wt%.

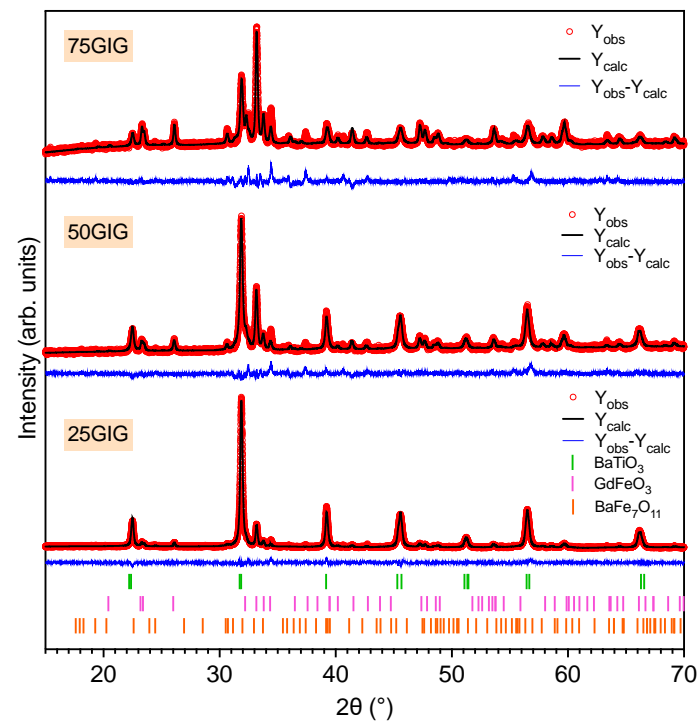


Figure 3. Rietveld refinement of the room temperature diffractogram from the powder composite samples.

Table 3. Results from the Rietveld refinement analysis for the composite samples.

Sample	BaTiO_3 (wt%)	GdFeO_3 (wt%)	$\text{BaFe}_7\text{O}_{11}$ (wt%)	R_{exp}	R_p	R_{wp}	χ
25GIG	84.24	15.04	0.72	3.83	3.70	4.95	1.29
50GIG	57.82	33.45	8.73	3.45	3.47	4.73	1.37
75GIG	26.44	55.42	18.14	2.51	2.67	3.91	1.56

3.3. Morphological Analysis

In Figure 4, produced by SEM, the cross-section micrographs can be observed of the BTO, GIG, and composite samples. In Figure 4a, almost a spherical shape of grains can be seen, with some agglomerates and a porous surface, characteristic of the BaTiO₃ crystal phase, similar to the results found in the literature [27]. The cross-section micrograph of the GIG sample in Figure 4b shows mostly grains with a uniform circular shape, along with some porosity, as described by Jiang L. et al. [28]. On the BTO and GIG micrographs (Figure 4a,b), porous surfaces are visible, with geometrical grains (grain joints are visible) and a homogenous grain size. Using the software Image J, we discerned an average grain size of 266 ± 34 nm for the BTO sample and 555 ± 98 nm for the GIG sample.

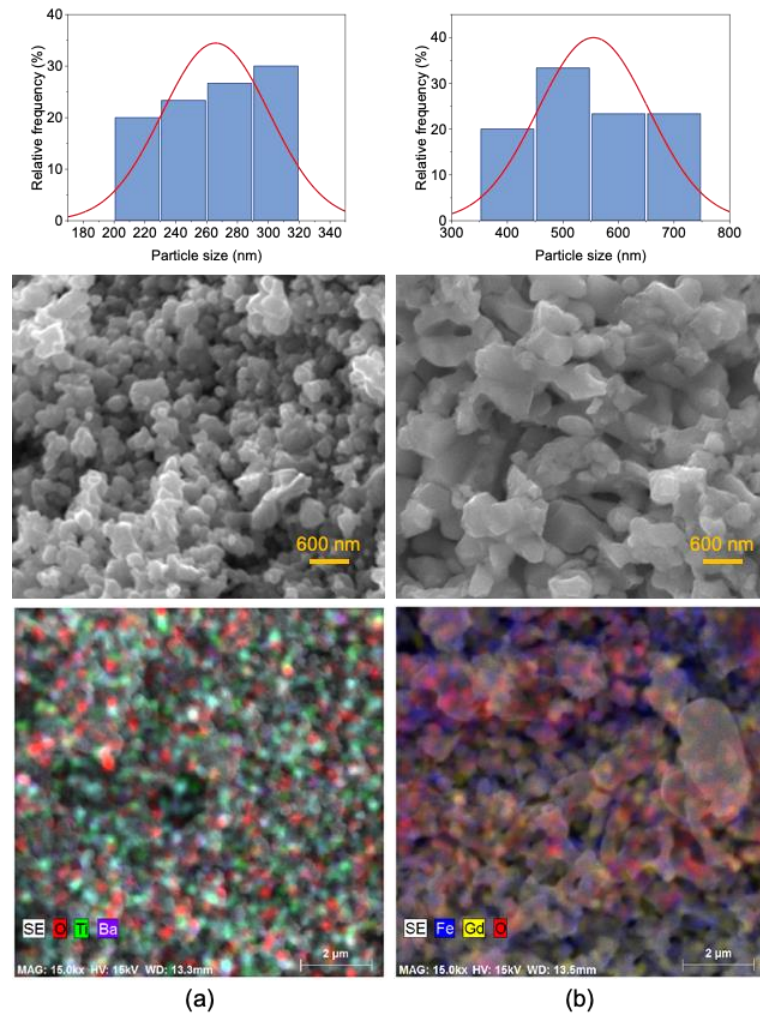


Figure 4. SEM micrography, grain size distribution, and EDS analysis of the cross-section of the samples, with a magnification of 30 k \times : (a) BTO and (b) GIG.

The cross-section micrographs of the composite samples can be found in Figure 5. The elemental analysis detected all expected elements, namely, Ba, Ti, O, Gd, and Fe. The EDS spectra of the composites did not reveal any unassigned peaks or contamination. With the addition of GIG in the BTO matrix, the average grain size increases from 262 ± 46 nm (25GIG) to 390 ± 72 nm (75GIG). This is related to the increased amount of the GdFeO₃ phase, which was found to exhibit larger particles (Figure 5d).

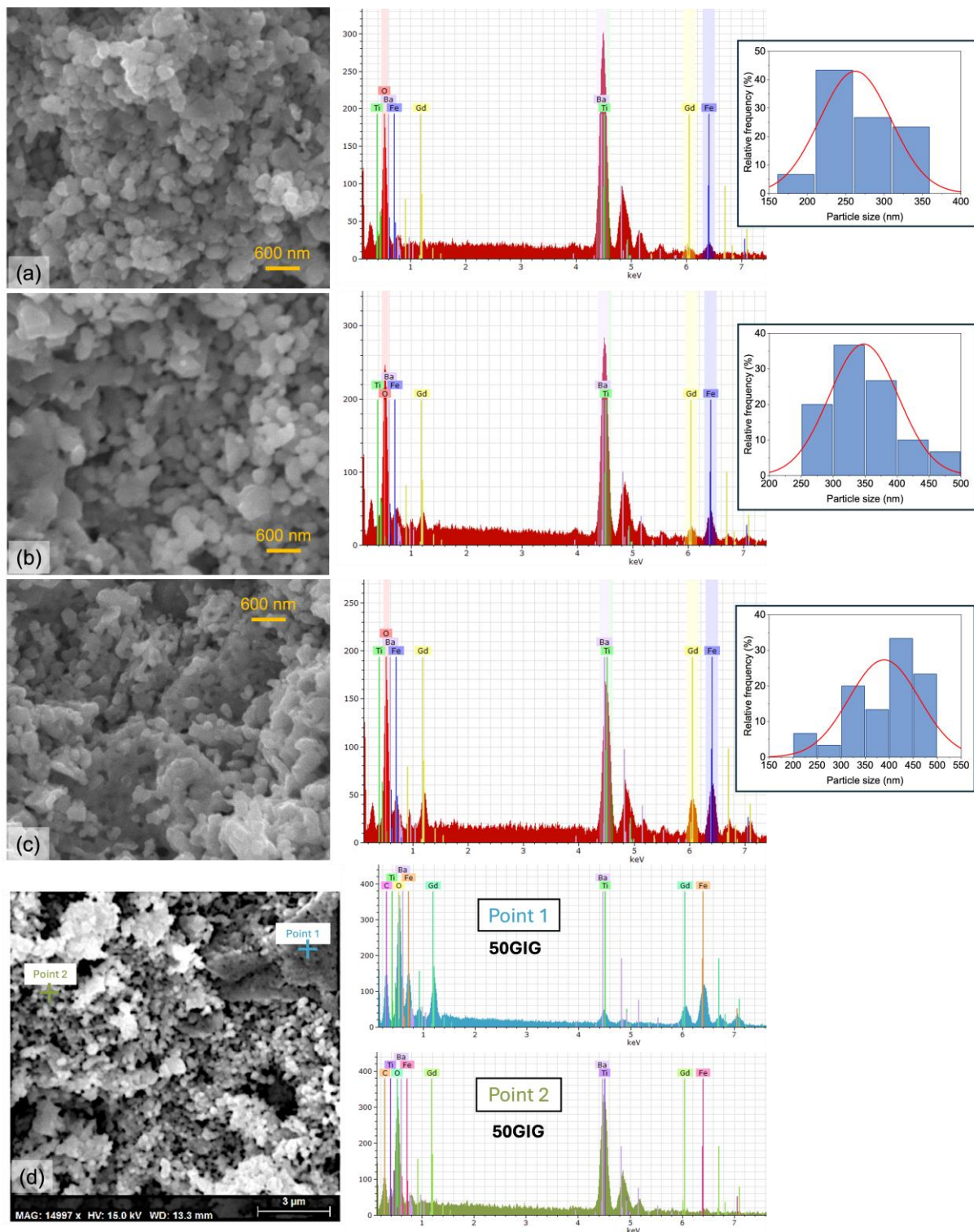


Figure 5. SEM micrography, grain size distribution, and EDS area analysis of the cross-section of the samples, with a magnification of 30 k \times : (a) 25 wt% GIG (25GIG), (b) 50 wt% GIG (50GIG), and (c) 75 wt% GIG (75GIG). (d) EDS point analysis of the 50 wt% GIG composite.

3.4. Electrical Analysis

3.4.1. Complex Permittivity

Figure 6 shows the dielectric constant of the BTO sample as a function of temperature, from 45 $^{\circ}$ C to 170 $^{\circ}$ C. This measurement was performed to complement the XRD results and evaluate the crystalline system obtained. As one can see, at around 120 $^{\circ}$ C, the

dielectric constant shows a discontinuity that could be suggestive of the tetragonal-to-cubic phase transition, which is known to occur around this temperature [20–22]. As for the absolute values of the dielectric constant, they are lower than that of the typical tetragonal ferroelectric BaTiO₃ samples. In addition to the low tetragonality of the BTO sample, this could be related to the small size of the BTO particles and/or the porosity of the pellet sample (Figure 4a). This observation could indicate that the heat treatment at 1000 °C was not sufficient to achieve high-quality BTO particles.

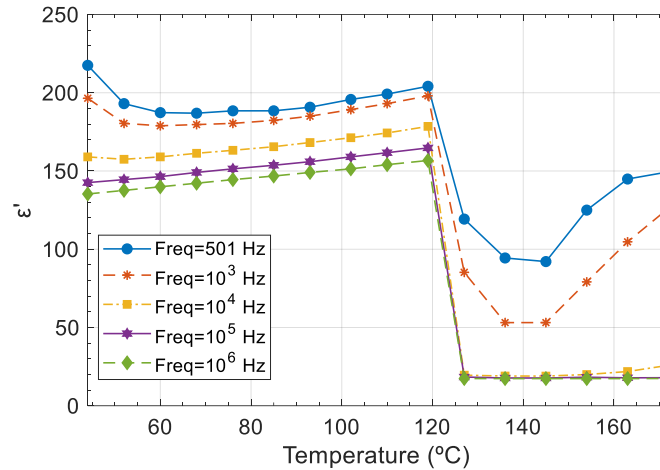


Figure 6. Dependence of the dielectric constant, ϵ' , on the temperature, at frequencies from 501 Hz to 10^6 Hz, for the BTO sample.

Figure 7a shows the real part of the complex permittivity, ϵ' , measured at room temperature, as a function of frequency. At lower frequencies, the dipolar polarization follows the time-varying electric field promoting an increase in the dielectric constant. As the frequency increases, the electrical dipoles are no longer able to keep the alignment with the electric field, leading to a decrease in the total polarization, which translates into a decrease in the dielectric constant. While historically, BTO was thought to be a displacive-type ferroelectric, there are more recent acknowledgments that it is a combination of displacive- and order–disorder-type materials [29–31].

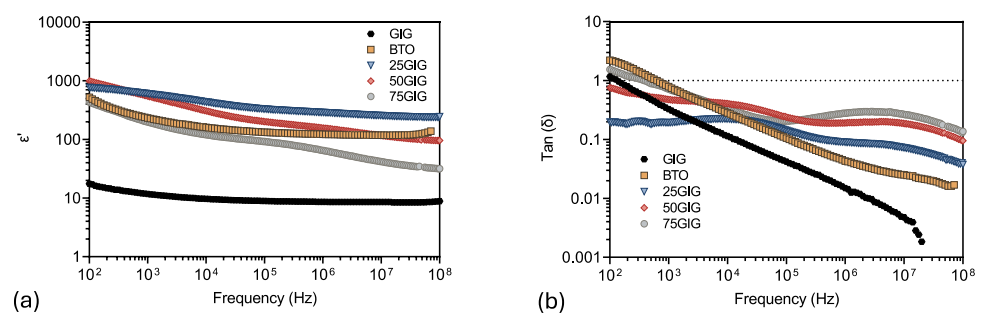


Figure 7. (a) Dielectric constant, ϵ' , and (b) $\text{Tan}(\delta)$ as a function of frequency for GIG, BTO, and composites with compositions of 25 wt% GIG (25GIG), 50 wt% (50GIG), and 75 wt% (75GIG).

The ϵ' of the GIG and BTO samples shows a plateau at higher frequencies. Therefore, one can take those values as a good estimate of the permittivity of the bulk. The GIG sample shows the lowest dielectric constant, with a value around 8 at 0.1 GHz. Meanwhile, for the BTO sample, the ϵ' value at high frequencies is around 119. The sample that exhibited the highest dielectric constant in comparison to the BTO sample could be attributed to either some charge carriers that are blocked at inner dielectric boundary layers, as explained by the Maxwell–Wagner–Sillars interfacial polarization, or the doping effect in BTO [32–35]. For

the 25GIG sampler, the ϵ' was close to 240, while having the loss tangent values (Figure 7b) below 1 in the entire frequency range. In fact, above 1 MHz, the loss tangent of this sample was below 0.1, making this the most interesting sample among the five for energy storage applications.

3.4.2. Electrical Modulus Formalism

For composite materials, impedance spectroscopy enables one to separate the contributions of different phases, using not only the formalisms of the complex permittivity, ϵ^* , but also of the complex electric modulus, M^* . These entities can be related as follows:

$$M^*(\omega) = \frac{1}{\epsilon^*(\omega)} = \frac{1}{\epsilon' - j\epsilon''} = \frac{\epsilon'}{(\epsilon'^2 + \epsilon''^2)} + j\frac{\epsilon''}{(\epsilon'^2 + \epsilon''^2)} \quad (1)$$

where $M'(\omega)$ and $M''(\omega)$ are the real and imaginary parts of the electrical modulus, which can be represented using the constant complex dielectric.

Figure 8 shows the variation in the imaginary part of M^* with frequency, at room temperature, for all samples. We can see the presence of at least one dielectric relaxation. To analyze these relaxation phenomena, we used an application software developed by the authors in MATLAB (part of that presented in [36]). In this way, the experimental data were adjusted by a multi-variable numerical simulation, which simultaneously fit the complex M^* and ϵ^* values using the Havriliak–Negami (HN) function:

$$M_{HN}^* = \frac{1}{\epsilon_{HN}^*} = \frac{1}{\epsilon_\infty + \sum_{k=1}^n \frac{\Delta\epsilon_k}{[1 + (j\omega\tau_k)^{\alpha_k}]^{\beta_k}} + \left(\frac{\sigma_{dc}}{j\omega\epsilon_0}\right)^s} \quad (2)$$

$$\epsilon_{HN}^*(\omega) = \epsilon_\infty + \sum_{k=1}^n \frac{\Delta\epsilon_k}{[1 + (j\omega\tau_k)^{\alpha_k}]^{\beta_k}} + \left(\frac{\sigma_{dc}}{j\omega\epsilon_0}\right)^s \quad (3)$$

where ϵ_∞ is the high-frequency limit of the dielectric permittivity, $\Delta\epsilon$ is the dielectric strength, τ_{HN} is the relaxation time from HN fitting, σ_{dc} represents the dc conductivity with ϵ_0 being the permittivity of the vacuum, s is a constant between 0 and 1, and α and β are shape factors ($0 \leq \alpha, \beta \leq 1$) related to the width and the asymmetry of curves, respectively. Depending on the α and β values, one can choose different models for the relaxation process. When $\alpha = \beta = 1$, the Debye model is obtained; for $\alpha \neq 0$ and $\beta = 1$, the dielectric relaxation follows the Cole–Cole (CC) model; and for $\alpha = 1$ and $\beta \neq 0$, the Cole–Davidson (CD) model is obtained. The purpose of using a multi-variable fitting algorithm is to find the optimal parameters for the Havriliak–Negami model, assuring that the result represents the relaxation phenomena in both formalisms, M^* and ϵ^* .

For the GIG and BTO samples, the M'' shows a single dielectric relaxation in the entire frequency range of analysis. From the HN fitting results (Table 4), one can use the relaxation frequency to estimate the capacitance of the process [37]:

$$C = \frac{C_0}{2 \cdot M''_{max}} \quad (4)$$

where M''_{max} is the corresponding M'' value at the relaxation frequency, and C_0 represents the capacitance of the empty cell, $C_0 = \epsilon_0 \frac{A}{L}$. The term A is the sample electrode contact area, and L is the sample's thickness.

According to our calculations, for the GIG sample, the capacitance of the relaxation is 4.02×10^{-12} F, while for the BTO sample, the capacitance is 6.14×10^{-11} F. These low capacitance values are typical for bulk processes, which suggests that for the GIG and BTO samples, the discussed relaxation is assigned to the bulk.

As for the composite samples, the electric modulus shows more than one relaxation phenomenon. For the 25GIG and 50GIG sample, three relaxation processes were identified, named low frequency (LF), intermediate frequency (IF), and high frequency (HF).

The high-frequency process is only observed for the composite samples, and its contribution becomes more prominent in the electric modulus as the wt% of GIG increases. This suggests that the HF process could be related to the bulk, most likely with the predominance of the GdFeO_3 grains since the amount of this phase also increases with the addition of GIG to the composites. The relaxation found at intermediate frequencies (IFs) should represent the combined response from the grain boundaries. As for the low-frequency process, its relaxation frequency appears to shift towards higher frequencies as the wt% of GIG increases. For the 25GIG and 50GIG samples, the relaxation frequency from this process is far apart from that of the IF process. However, for the 75GIG sample, there seems to be a convolution of the LF and IF processes; hence, we can only identify two relaxation processes, one at intermediate frequencies and the HF process. The LF relaxation should be related to a nonohmic process at the sample/electrode interface.

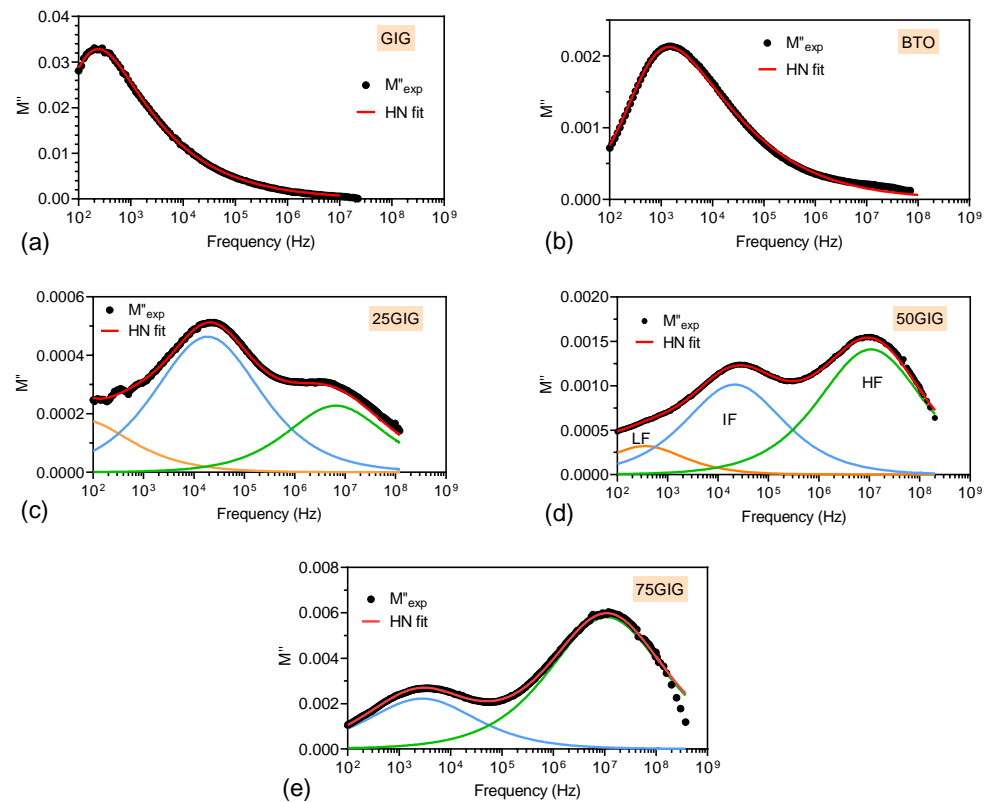


Figure 8. Dependence of the imaginary part of the electric Modulus, M'' , on the frequency and the fit according to the simulation using the Havriliak–Negami (HN) model (red curve) for (a) GIG, (b) BTO, and composites with (c) 25 wt% of GIG, (d) 50 wt% of GIG, and (e) 75 wt% of GIG.

Table 4. Havriliak–Negami parameters from the numerical fitting to the M^* and ϵ^* data of the samples.

	$\Delta\epsilon_{\text{HN}_{\text{LF}}}$	$\Delta\epsilon_{\text{HN}_{\text{IF}}}$	$\Delta\epsilon_{\text{HN}_{\text{HF}}}$	$\epsilon_{\infty_{\text{LF}}}$	$\epsilon_{\infty_{\text{IF}}}$	$\epsilon_{\infty_{\text{HF}}}$	$f_{M''_{\text{max}}_{\text{LF}}}$ (Hz)	$f_{M''_{\text{max}}_{\text{IF}}}$ (Hz)	$f_{M''_{\text{max}}_{\text{HF}}}$ (Hz)	σ (S/m)
GIG	23.7			8.4			360			7.97×10^{-8}
BTO	663.8			114.2			2734			5.47×10^{-6}
25GIG	661.5	378.0	59.7	669.1	291.1	231.4	52	18,700	6.5×10^6	6.97×10^{-8}
50GIG	867.0	412.2	90.4	589.7	177.5	87.0	356	21,290	1.1×10^7	2.41×10^{-6}
75GIG		914.1	69.5		97.2	27.7		2810	1.1×10^7	2.55×10^{-6}

The Nyquist M^* plots of the samples are shown in Figure 9. For all samples, the obtained HN fit agrees very well with the experimental data. The analysis of the complex

function is very important since the shape of dielectric relaxation can only be fully characterized when the HN model is fitted to the complex M^* or ϵ^* function. In addition, to determine the dielectric strength ($\Delta\epsilon$), the fitting model requires the M' or ϵ' values, since $\Delta\epsilon = \epsilon_s - \epsilon_\infty$.

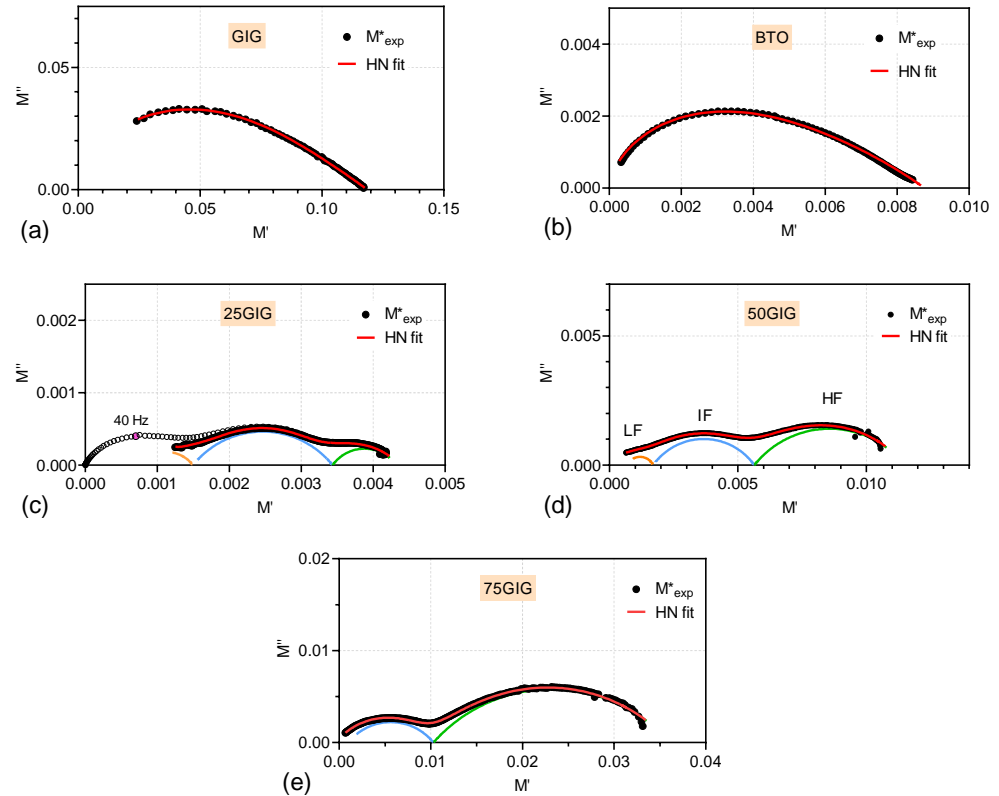


Figure 9. Nyquist plot, M'' vs. M' , and the fit according to the simulation using the Havriliak–Negami (HN) model (red curve) for (a) GIG, (b) BTO, and composites (c) 25GIG, (d) 50GIG, and (e) 75GIG.

The GIG and BTO samples (Figure 8) show an asymmetric curve characteristic of the Cole–Davidson model. In fact, for both samples, the obtained shape parameters of the HN function were $\alpha = 1$ and $\beta = 0.4$. As for the composite samples, the experimental M^* data were fitted using multiple Cole–Cole relaxations. For the 25GIG sample (Figure 8), one supplementary impedance measurement was taken up to lower frequencies (0.01 Hz), to inspect if any additional relaxation occurred beyond the LF process. The data from this measurement, plotted as open circles in Figure 9, confirm that the LF relaxation intersects the origin of the electric modulus; hence, no additional relaxation is observed.

As previously discussed, the dielectric relaxations were investigated by simultaneously fitting the complex M^* and ϵ^* values to the Havriliak–Negami (HN) function. Figure 10 shows the complex permittivity of the 25GIG sample, revealing the three relaxation processes, and that the HN parameters are well suited to both formalisms (M^* and ϵ^*). While in the M'' representation, the contribution of the HF process is large and becomes the dominant process for the 50GIG and 75GIG samples, the intensity of this relaxation is much smaller in the complex permittivity representation. The electric modulus has the advantage of minimizing high capacitance effects such as spatial charge accumulation effects [38], which allows small capacitance processes to be disclosed and highlighted, such as localized dipole relaxations in the bulk. As shown in Table 4, the dielectric strength of this process ($\Delta\epsilon_{\text{HN}_{\text{HF}}}$) is also the smallest among the three relaxations, which corroborates its smaller intensity in the Nyquist ϵ^* plot.

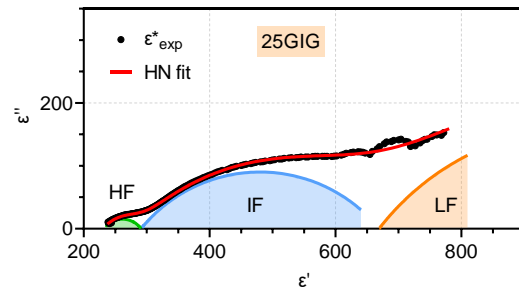


Figure 10. Cole–Cole plot for composite of 25 wt% of GIG and the adjustment according to the simulation using the Havriliak–Negami (HN) model (red curve), showing three relaxation processes.

3.4.3. Impedance Response

The electrical properties of the samples were further studied using the impedance formalism. The analysis using equivalent circuit models (ECMs) allowed us to identify the contributions observed in the impedance spectrum based on their resistance and capacitance. The distinction between different electrochemical processes could be determined based on the order of magnitudes of their capacitances.

Figure 11 shows the Nyquist Z^* plot of the GIG sample. The impedance data of this sample were fitted to an electrical circuit consisting of a resistor (R_1) in parallel with a constant phase element (CPE_1), using MATLAB application software developed by the authors [39]. From the fit results, we calculated the true capacitance of the constant phase element with the Brug formula [40,41] and a value of 4.5×10^{-12} F was obtained (Table 5). This value is in good agreement with the capacitance calculated using the M''_{max} value, confirming that the constant phase element represents the bulk capacitance and the resistor the bulk resistance. Both depend on the sample's geometry. The bulk conductivity was also calculated and the obtained value, 9.36×10^{-8} S/m, is also very close to the σ_{DC} value obtained from the HN fitting (7.97×10^{-8} S/m).

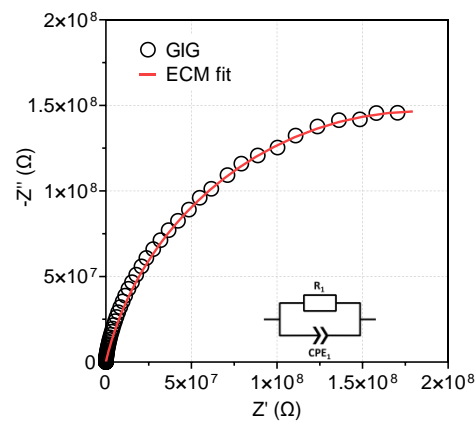


Figure 11. Nyquist plot, $-Z''$ vs. Z' , for the GIG sample at room temperature. The inset of the graphic shows the equivalent circuit model (ECM) used to fit the data.

The impedance data of the BTO sample (Figure 12) could not be modeled by a single $R//CPE$ circuit; hence, the equivalent circuit model of choice was a resistor (R_1) in parallel with a constant phase element (CPE_1), connected in series with a second resistor (R_2) in parallel with a constant phase element (CPE_2). The impedance at a low frequency clearly suggests a second semicircle that extends to lower frequencies, beyond our frequency range of analysis. The capacitance of the low-frequency semicircle ($R_2//CPE_2$) is 1.5×10^{-9} F, which indicates that this relaxation process is assigned to the grain boundaries. The high-frequency semicircle, represented by $R_1//CPE_1$, is associated with the bulk. The total conductivity of the sample, calculated with the resistance from the bulk and grain boundary, is 3.93×10^{-6} S/m, which also corroborates with the HN result. This agreement highlights

the effectiveness of our approach using a multi-variable algorithm with simultaneous fitting of the complex M^* and ϵ^* values.

Table 5. Obtained parameters from the equivalent circuit model of the impedance of the samples.

	R_1 (Ω)	C_1 (F)	R_2 (Ω)	C_2 (F)	σ (S/m)
GIG	3.7×10^8	4.5×10^{-12}			9.36×10^{-8}
BTO	4.6×10^6	7.5×10^{-11}	4.0×10^6	1.5×10^{-9}	3.93×10^{-6}
25GIG	4.0×10^8	3.5×10^{-10}			8.36×10^{-8}
50GIG	1.9×10^7	4.0×10^{-10}			1.84×10^{-6}
75GIG	1.4×10^7	1.2×10^{-10}			2.54×10^{-6}

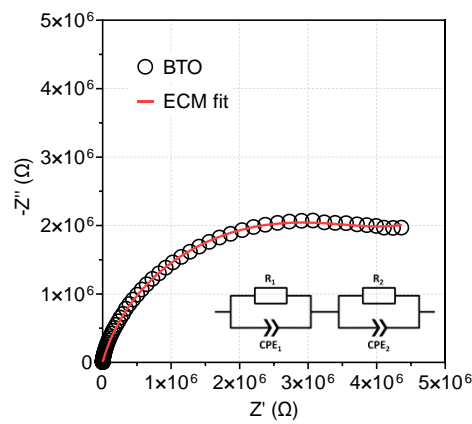


Figure 12. Nyquist plot, $-Z''$ vs. Z' , for the BTO sample at room temperature. The inset of the graphic shows the equivalent circuit model (ECM) used to fit the data.

Similarly to the GIG sample (Figure 10), the impedance of the composite samples shows an incomplete semicircle (Figure 13) that is well-fitted to an electrical circuit consisting of a resistor (R_1) in parallel with a constant phase element (CPE_1). As shown in Table 5, the conductivity of the 75GIG and 50GIG samples is very close, at 2.54×10^{-6} S/m and 1.84×10^{-6} S/m, respectively. Conversely, for the 25GIG sample, the conductivity is two orders of magnitude lower, at 8.36×10^{-8} S/m. When judging solely on the capacitance values (around 10^{-10} F), one cannot accurately conclude on the assignment of this contribution. Although they resemble the typical values found for grain boundaries (10^{-11} – 10^{-8} F), additional information such as impedance measurements as a function of temperature is required to confirm this assumption.

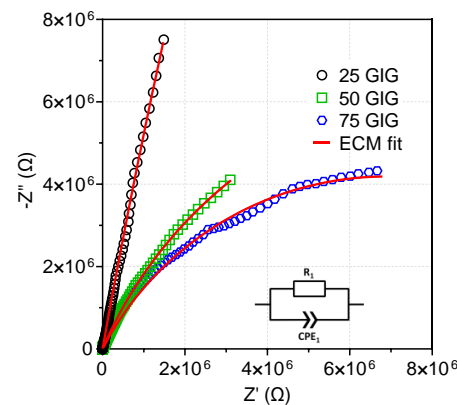


Figure 13. Nyquist plot, $-Z''$ vs. Z' , for the composites' 25GIG, 50GIG, and 75GIG samples at room temperature. The inset of the graphic shows the equivalent circuit model (ECM) used to fit the data.

4. Conclusions

In the present work, we studied the dielectric and structural properties of barium titanate–gadolinium ferrite composite samples. The composites were found to be a mixture of three crystal phases, BaTiO₃, GdFeO₃, and BaFe₇O₁₁. The weight percentage of the GdFeO₃ perovskite structure was found to increase with the addition of GIG to the composites, by up to 55 wt% for the 75GIG sample. According to the diffractogram of the BTO sample, the synthesized powder crystallized in the tetragonal phase, although it can be concluded that the single-step sintering procedure used is not effective in achieving BTO particles with a high tetragonality, possibility due to the low annealing temperature and/or the annealing time and atmosphere used. As for the GIG powder, the XRD analysis showed that the main phase is Gd₃Fe₅O₁₂ (81 wt%).

The dielectric relaxations of the samples were modeled according to the Havriliak–Negami function. For the GIG and BTO samples, the electric modulus exhibited a single relaxation, which was assigned to a localized relaxation process within the bulk. The 25GIG and 50GIG samples showed three relaxation processes, whereas for the 75GIG sample, only two dielectric relaxations could be observed.

The conductivity of the samples, the dielectric constant, and the loss tangent were also studied. The sample with the highest dielectric constant was the 25GIG composite, with an ϵ' close to 240 and loss tangent values below 0.1. In comparison to the remaining samples, this composition showed the most appealing features for energy storage applications.

This work also reports a new fitting procedure for studying the dielectric relaxations of materials using the Havriliak–Negami function. The use of a multi-variable numerical algorithm that simultaneously fits complex M^* and ϵ^* values was found to effectively provide the general solution to both immittance functions. Moreover, the conductivity values obtained from the Havriliak–Negami function in this approach showed a very good agreement with those obtained from the conventional method, namely, impedance fitting with equivalent circuits.

Author Contributions: Conceptualization, R.B., D.F. and L.C.; methodology, B.M.G.M., C.B. and R.B.; software, B.M.G.M.; validation, D.F., S.S.T. and M.P.F.G.; formal analysis, C.B.; investigation, B.M.G.M., C.B. and R.B.; data curation, B.M.G.M., C.B. and S.S.T.; writing—original draft, B.M.G.M., C.B., R.B., S.S.T. and L.C.; writing—review and editing, B.M.G.M., D.F., S.S.T., M.P.F.G. and L.C.; supervision, R.B., D.F. and L.C.; project administration, M.P.F.G.; funding acquisition, M.P.F.G. and L.C. All authors have read and agreed to the published version of the manuscript.

Funding: This research was funded by i3N (LA/P/0037/2020, UID-B/50025/2020, and UID-P/50025/2020) financed by the COMPETE 2020 Program and national funds through FCT/MEC and FEDER under the PT2020 Partnership Agreement. This work was also funded by national funds (OE), through FCT—Fundação para a Ciência e a Tecnologia, I.P., in the scope of the framework contract foreseen in numbers 4, 5, and 6 of article 23, of the Decree-Law 57/2016, of 29 August, changed by Law 57/2017, of 19 July.

Data Availability Statement: The original contributions presented in the study are included in the article, further inquiries can be directed to the corresponding author.

Conflicts of Interest: The authors declare no conflict of interest.

References

1. McKubre, M.C.H.; Macdonald, D.D. Impedance Measurement Techniques and Data Analysis. In *Impedance Spectroscopy Theory, Experiment, and Applications*; Barsoukov, E., Macdonald, J.R., Eds.; John Wiley & Sons, Inc.: Hoboken, NJ, USA, 2005; Volume 177, p. 606, ISBN 0-471-64749-7.
2. Yuan, Y.; Lin, J.; Wang, X.; Qian, J.; Zuo, P.; Zhuang, Q. Achieving Excellent Dielectric and Energy Storage Performance in Core-Double-Shell-Structured Polyetherimide Nanocomposites. *Polymers* **2023**, *15*, 3088. [[CrossRef](#)] [[PubMed](#)]
3. Tang, H.; Zhou, Z.; Bowland, C.C.; Sodano, H.A. Synthesis of Calcium Copper Titanate (CaCu₃Ti₄O₁₂) Nanowires with Insulating SiO₂ Barrier for Low Loss High Dielectric Constant Nanocomposites. *Nano Energy* **2015**, *17*, 302–307. [[CrossRef](#)]
4. Lu, J.; Wong, C.P. Recent Advances in High-k Nanocomposite Materials for Embedded Capacitor Applications. *IEEE Trans. Dielectr. Electr. Insul.* **2008**, *15*, 1322–1328. [[CrossRef](#)]

5. Li, W.-B.; Zhou, D.; Pang, L.-X.; Xu, R.; Guo, H.-H. Novel Barium Titanate Based Capacitors with High Energy Density and Fast Discharge Performance. *J. Mater. Chem. A* **2017**, *5*, 19607–19612. [[CrossRef](#)]
6. Acosta, M.; Novak, N.; Rojas, V.; Patel, S.; Vaish, R.; Koruza, J.; Rossetti, G.A.; Rödel, J. BaTiO₃-Based Piezoelectrics: Fundamentals, Current Status, and Perspectives. *Appl. Phys. Rev.* **2017**, *4*, 041305. [[CrossRef](#)]
7. Dong, X.; Li, X.; Chen, H.; Sun, C.; Shi, J.; Pang, F.; Chen, X.; Zhou, H. Effective Strategy to Realise Excellent Energy Storage Performances in Lead-Free Barium Titanate-Based Relaxor Ferroelectric. *Ceram. Int.* **2021**, *47*, 6077–6083. [[CrossRef](#)]
8. Mi, L.; Zhang, Q.; Wang, H.; Wu, Z.; Guo, Y.; Li, Y.; Xiong, X.; Liu, K.; Fu, W.; Ma, Y.; et al. Synthesis of BaTiO₃ Nanoparticles by Sol-Gel Assisted Solid Phase Method and Its Formation Mechanism and Photocatalytic Activity. *Ceram. Int.* **2020**, *46*, 10619–10633. [[CrossRef](#)]
9. Hu, J.; Chen, L.; Nan, C. Multiferroic Heterostructures Integrating Ferroelectric and Magnetic Materials. *Adv. Mater.* **2016**, *28*, 15–39. [[CrossRef](#)] [[PubMed](#)]
10. Hao, Y.; Li, Y.; Yao, X.; Wang, X. Studies of Ferroelectric and Dielectric Properties of Samarium Doped Barium Titanate Sintered in Pure Nitrogen. *Ferroelectrics* **2010**, *407*, 146–153. [[CrossRef](#)]
11. Morrison, F.D.; Sinclair, D.C.; West, A.R. Alternative Explanation for the Origin of the Resistivity Anomaly in La-Doped BaTiO₃. *J. Am. Ceram. Soc.* **2001**, *84*, 474–476. [[CrossRef](#)]
12. Zhang, K.; Li, L.; Wang, M.; Luo, W. Charge Compensation in Rare Earth Doped BaTiO₃-Based Ceramics Sintered in Reducing Atmosphere. *Ceram. Int.* **2020**, *46*, 25881–25887. [[CrossRef](#)]
13. Ren, P.; He, J.; Wang, X.; Sun, M.; Zhang, H.; Zhao, G. Colossal Permittivity in Niobium Doped BaTiO₃ Ceramics Annealed in N₂. *Scr. Mater.* **2018**, *146*, 110–114. [[CrossRef](#)]
14. Li, Z.; Yu, J.; Hao, S.; Janolin, P.E. Enhancing Properties of Lead-Free Ferroelectric BaTiO₃ through Doping. *J. Eur. Ceram. Soc.* **2022**, *42*, 4693–4701. [[CrossRef](#)]
15. Xiao, Y.; Yang, Y.; Yang, S.; Li, J.; Liu, D.; Wu, J.; Wang, M.; Li, C.; Li, F. Simultaneous Enhancement of Dielectric Properties and Temperature Stability in BaTiO₃-Based Ceramics Enabling X8R Multilayer Ceramic Capacitor. *Int. J. Appl. Ceram. Technol.* **2023**, *20*, 3735–3742. [[CrossRef](#)]
16. Soreto Teixeira, S.; Sales, A.J.M.; Graça, M.P.F.; Costa, L.C. Yttrium Ferrites with Enhanced Dielectric Properties. *Mater. Sci. Eng. B* **2018**, *232–235*, 41–47. [[CrossRef](#)]
17. Qi, J.; Zhang, M.; Chen, Y.; Luo, Z.; Zhao, P.; Su, H.; Wang, J.; Wang, H.; Yang, L.; Pan, H.; et al. High-Entropy Assisted BaTiO₃-Based Ceramic Capacitors for Energy Storage. *Cell Rep. Phys. Sci.* **2022**, *3*, 101110. [[CrossRef](#)]
18. Baivier, C.; Hammami, I.; Benzerger, R.; Graça, M.P.F.; Costa, L.C. Barium Titanate/Gadolinium Ferrite: A New Material Composite to Store Energy. *Nanomaterials* **2023**, *13*, 1955. [[CrossRef](#)]
19. Grousseau, P. Synthèse et Étude Du Grenat de Fer et D'yttrium. Ph.D. Thesis, Ecole Nationale Supérieure des Mines de Saint-Etienne, Saint-Étienne, France, 1993.
20. Raza, S.A.; Awan, S.U.; Hussain, S.; Shah, S.A.; Iqbal, A.M.; Khurshid Hasanain, S. Structural, Ferromagnetic, Electrical, and Dielectric Relaxor Properties of BaTiO₃ and CoFe₂O₄ Bulk, Nanoparticles, and Nanocomposites Materials for Electronic Devices. *J. Appl. Phys.* **2020**, *128*, 124101. [[CrossRef](#)]
21. Rached, A.; Wederni, M.A.; Khirouni, K.; Alaya, S.; Martín-Palma, R.J.; Dhahri, J. Structural, Optical and Electrical Properties of Barium Titanate. *Mater. Chem. Phys.* **2021**, *267*, 124600. [[CrossRef](#)]
22. Sareecha, N.; Ali Shah, W.; Anis-ur-Rehman, M.; Latif Mirza, M.; Awan, M.S. Electrical Investigations of BaTiO₃ Ceramics with Ba/Ti Contents under Influence of Temperature. *Solid. State Ion.* **2017**, *303*, 16–23. [[CrossRef](#)]
23. Yoon, D. Tetragonality of Barium Titanate Powder for a Ceramic Capacitor Application. *J. Ceram. Process. Res.* **2006**, *7*, 343.
24. Ryu, S.-S.; Yoon, D.-H. Solid-State Synthesis of Nano-Sized BaTiO₃ Powder with High Tetragonality. *J. Mater. Sci.* **2007**, *42*, 7093–7099. [[CrossRef](#)]
25. Kong, L.B.; Ma, J.; Huang, H.; Zhang, R.F.; Que, W.X. Barium Titanate Derived from Mechanochemically Activated Powders. *J. Alloys Compd.* **2002**, *337*, 226–230. [[CrossRef](#)]
26. Kim, J.-H.; Jung, W.-S.; Kim, H.-T.; Yoon, D.-H. Properties of BaTiO₃ Synthesized from Barium Titanate Oxalate. *Ceram. Int.* **2009**, *35*, 2337–2342. [[CrossRef](#)]
27. Vijatovic, M.; Vasic, M.; Bobic, J.; Zivkovic, L.; Stojanovic, B. Effect of Powder Synthesis Method on BaTiO₃ Ceramics. *Process. Appl. Ceram.* **2008**, *2*, 27–31. [[CrossRef](#)]
28. Jiang, L.; Yang, S.; Zheng, M.; Chen, H.; Wu, A. Synthesis and Magnetic Properties of Nanocrystalline Gd₃Fe₅O₁₂ and GdFeO₃ Powders Prepared by Sol-Gel Auto-Combustion Method. *Mater. Res. Bull.* **2018**, *104*, 92–96. [[CrossRef](#)]
29. Diao, J.; Robinson, I.K. Ferroelectric Domains in Barium Titanate by Bragg Coherent X-ray Diffraction Imaging. Ph.D. Thesis, University College London, London, UK, 2022.
30. Wang, J.; Jin, K.; Yao, H.; Gu, J.; Xu, X.; Ge, C.; Wang, C.; He, M.; Yang, G. Temperature-Dependent Phase Transition in Barium Titanate Crystals Probed by Second Harmonic Generation. *Appl. Phys. Lett.* **2018**, *112*, 102904. [[CrossRef](#)]
31. Stern, E.A. Character of Order-Disorder and Displacive Components in Barium Titanate. *Phys. Rev. Lett.* **2004**, *93*, 037601. [[CrossRef](#)] [[PubMed](#)]
32. Deng, J.; Han, F.; Schwarz, B.; Knapp, M.; Ehrenberg, H.; Hua, W.; Hinterstein, M.; Li, G.; He, Y.; Wang, J.; et al. Dielectric Relaxation and Magnetic Structure of A-Site-Ordered Perovskite Oxide Semiconductor CaCu₃Fe₂Ta₂O₁₂. *Inorg. Chem.* **2021**, *60*, 6999–7007. [[CrossRef](#)] [[PubMed](#)]

33. Meng, Y.; Liu, K.; Zhang, X.; Lei, X.; Chen, J.; Yang, Z.; Peng, B.; Long, C.; Liu, L.; Li, C. Defect Engineering in Rare-Earth-Doped BaTiO₃ Ceramics: Route to High-Temperature Stability of Colossal Permittivity. *J. Am. Ceram. Soc.* **2022**, *105*, 5725–5737. [[CrossRef](#)]
34. Meng, Y.; Liu, K.; Zhang, X.; Qiang, X.; Lei, X.; Chen, J.; Li, C.; Yang, Z.; Liu, L. Compositional Modulation and Annealing Treatment in BaTiO₃ to Simultaneously Achieve Colossal Permittivity, Low Dielectric Loss, and High Thermal Stability. *Ceram. Int.* **2021**, *47*, 33912–33916. [[CrossRef](#)]
35. Liu, L.; Ren, S.; Zhang, J.; Peng, B.; Fang, L.; Wang, D. Revisiting the Temperature-Dependent Dielectric Permittivity of Ba(Ti_{1-x}Zr_x)O₃. *J. Am. Ceram. Soc.* **2018**, *101*, 2408–2416. [[CrossRef](#)]
36. Melo, B.M.G.; Loureiro, F.J.A.; Fagg, D.P.; Costa, L.C.; Graça, M.P.F. DFRTtoEIS: An Easy Approach to Verify the Consistency of a DFRT Generated from an Impedance Spectrum. *Electrochim. Acta* **2021**, *366*, 137429. [[CrossRef](#)]
37. Abrantes, J.C.C.; Feighery, A.; Ferreira, A.A.L.; Labrincha, J.A.; Frade, J.R. Impedance Spectroscopy Study of Niobium-Doped Strontium Titanate Ceramics. *J. Am. Ceram. Soc.* **2004**, *85*, 2745–2752. [[CrossRef](#)]
38. Graça, M.P.F.; Melo, B.M.G.; Prezas, P.R.; Valente, M.A.; Freire, F.N.A.; Bih, L. Electrical and Dielectric Analysis of Phosphate Based Glasses Doped with Alkali Oxides. *Mater. Des.* **2015**, *86*, 427–435. [[CrossRef](#)]
39. EIS Smart Tool. Available online: <https://github.com/bmgmelo/EIS-smart-tool> (accessed on 21 June 2024).
40. Melo, B.M.G.; Blaskova-Kochnitcharova, D.; Teixeira, S.S.; Lefterova, E.; Petkov, P.; Petkova, T.; Costa, L.C. Relaxation Processes in TiO₂-V₂O₅-P₂O₅ Glass-Ceramics. *Ceram. Int.* **2021**, *47*, 29047–29054. [[CrossRef](#)]
41. Shoar Abouzari, M.R.; Berkemeier, F.; Schmitz, G.; Wilmer, D. On the Physical Interpretation of Constant Phase Elements. *Solid. State Ion.* **2009**, *180*, 922–927. [[CrossRef](#)]

Disclaimer/Publisher’s Note: The statements, opinions and data contained in all publications are solely those of the individual author(s) and contributor(s) and not of MDPI and/or the editor(s). MDPI and/or the editor(s) disclaim responsibility for any injury to people or property resulting from any ideas, methods, instructions or products referred to in the content.